Band Bending and Ratcheting Explain Triboelectricity in a Flexoelectric Contact Diode

Karl P. Olson, Christopher A. Mizzi, and Laurence D. Marks*

ACCESS | Metrics & More | Article Recommendations | Supporting Information

ABSTRACT: Triboelectricity was recognized millennia ago, but the fundamental mechanism of charge transfer is still not understood. We have recently proposed a model where flexo-electric band bending due to local asperity contacts drives triboelectric charge transfer in non-metals. While this ab initio model is consistent with a wide range of observed phenomena, to date there have been no quantitative analyses of the proposed band bending. In this work we use a $Pt_{0.8}Ir_{0.2}$ conductive atomic force microscope probe to simultaneously deform a Nb-doped $SrTiO_3$ sample and collect current−bias data. The current that one expects based upon an analysis including the relevant flexoelectric band bending for a deformed semiconductor quantitively agrees with the experiments. The analysis indicates a general ratcheting mechanism for triboelectric transfer and strong experimental evidence that flexoelectric band bending is of fundamental importance for triboelectric contacts.

KEYWORDS: *Flexoelectricity, Triboelectricity, Band structures, Schottky diodes, Contact mechanics*
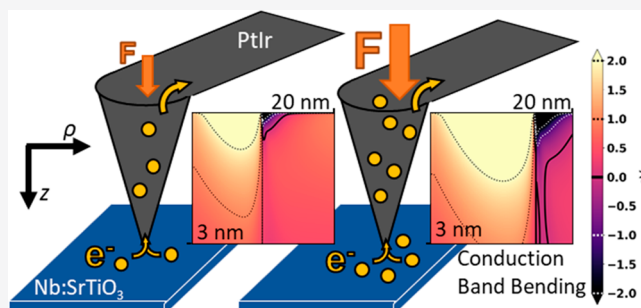
Triboelectricity is a phenomenon of importance in areas ranging from the processing of pharmaceutical powders,[1−3] nanoscale energy harvesting,[4−9] and the electrification of blowing sand, snow, or volcanic plumes[10−14] to damaging of wind turbines,[15] combing human hair[16,17] and even planetary formation.[18] It occurs whenever two materials rub together or discrete particles collide—the latter is often called contact or granular electrification.

The current literature includes older experiments, where hypotheses such as the "triboelectric series" were shown to be false,[19−24] to recent, specialized work which sometimes misses the earlier results. It is generally accepted that the triboelectric effect depends upon transfer of electrons,[25−27] ions,[28,29] and/ or charged molecular fragments.[30] One common idea is that differences in the work function drive charge transfer, the Volta−Helmholtz hypothesis.[21] As summarized in 1967 by Harper,[24] this fails to explain many experimental observations, for instance that charging can occur when two pieces of the same material are rubbed against each other. While work function differences matter, alone they do not explain triboelectricity. For many decades the missing terms have been unknown, despite numerous applications.

We have recently[31] argued that the missing term is the flexoelectric effect, the coupling of strain gradients during asperity contacts and polarization, and subsequently extended the analysis to include local band bending.[32] To move the field forward requires rigorously testing the connection between flexoelectricity and triboelectricity, performing a quantitative experimental and theoretical analysis of the band bending

during asperity contact including the electromechanical terms and others such as work function differences and semiconductor depletion regions.

Such an analysis has many components, some of which are already partially understood. An experimental approach was demonstrated in the early works of Terris et al.[33] and Jeffery et al.,[34] which showed that forces applied using a conductive atomic force microscope (CAFM) probe changed the local electronic structure. For a metal in contact with a semiconductor, in 1953 Vick[35] pointed out the importance of Schottky barriers, while in 1967 Harper[24] analyzed the triboelectric importance of the band bending. There are potentials created by indentation which have been analyzed for piezoelectric,[36] and more recently flexoelectric[31,32,37,38] materials. Other aspects have been analyzed such as the variation of the effective barrier for an indentation Schottky diode by Sun et al.[38] Other works[39−42] have calculated the flexoelectric polarization or field and noted their importance in triboelectric contacts; for instance, sliding Schottky energy-harvesting devices.[8,43−46] Despite extensive efforts, no work has been able to develop a complete theory that quantitatively
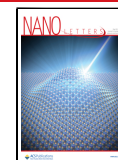
agrees with experiment for the flexoelectric case. (Note that only a small number of materials are piezoelectric, and for materials such as quartz, piezoelectricity is not important for triboelectricity.[24]) A review of flexoelectric AFM experiments has recently been published that covers many aspects.[47] However, as will become apparent herein, the problem is more complex than the existing literature analysis with terms such as the mean inner potential[48] omitted.

In this Letter, we develop a detailed band-bending model that quantitatively agrees with the force-dependent current−bias ($I−V$) behavior in a CAFM Schottky diode between a $Pt_{0.8}Ir_{0.2}$ (PtIr) tip and Nb-doped strontium titanate (STO). The model follows conventional semiconductor analyses,[49,50] taking into account depletion layers and image forces. A Hertzian model[51] for strains and strain gradients is used for flexoelectric and strain-dependent terms that consider the shift of the mean inner potential. Simple but appropriate models for transport are used to connect the band-bending to experimental data for both forward and reverse bias. The analysis contains only two adjustable parameters, namely, the ideality factor of the diode and the height of the Schottky barrier, which we fit from the experimental data. Other relevant parameters are either known or calculated ab initio. Upon the basis of the analysis we can also explain why the current transfer in sliding Schottky generator experiments[43,52] is surprisingly weakly dependent upon exact details of flexocoupling coefficient signs, as well as shear versus tensile contributions during contacts. We argue that the experimental verification of the theoretical analysis strongly indicates a significant if not dominant role for flexoelectricity in triboelectricity.

Figure 1 shows the $I−V$ characteristics of the PtIr−STO system with applied force, F, for both forward and reverse bias.
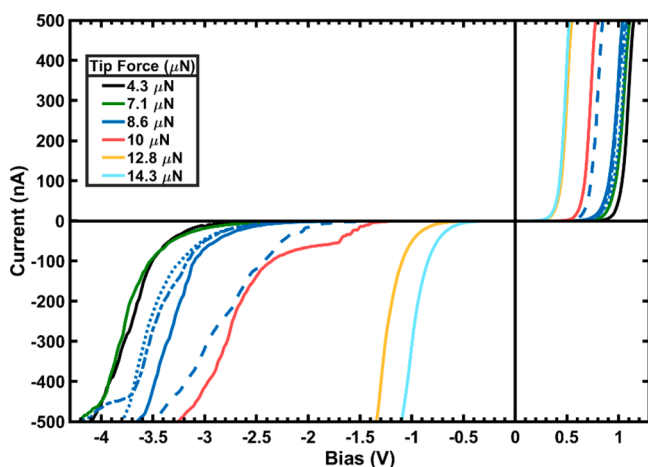

Figure 1. Experiemenial $I−V$ data for a $Pt_{0.8}Ir_{0.2}$ AFM tip contacting an 0.7% Nb-doped $SrTiO_3$ sample. Colors indicate different forces, with the current generally increasing toward no bias. Four repeated, but nonconsecutive, measurements we collected at each tip force; the line styles for the 8.6 μN data represent a typical set. For clarity, the remaining repetitions and some tip forces are omitted (see the Supporting Information (Section SN3) for complete data).

Increasing force shifted the bias at which a significant current was observed in all cases.

We will first analyze the forward bias. Without any force, the system behaves as a Schottky diode with the Fermi level of the semiconductor pinned by defect states, where the pinning is with respect to the metal. (For completeness, an analysis with pinning a fixed energy difference with respect to the semiconductor states is in the Supporting Information (Section SN9) and is not close to the experiment.) The band structure of the zero-force case is illustrated in Figure 2. Under forward
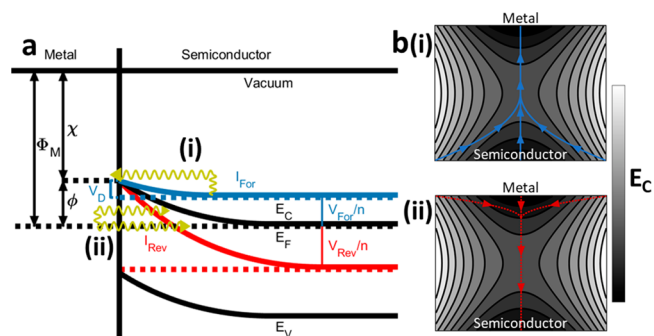

Figure 2. Band-bending diagram and electron path schematics. (a) Band diagram corresponding to the experimental setup under no strain. The metal tip is on the left, and the semiconductor is on the right. The barrier height, ϕ, is the difference between the metal work function, Φ_m, and the semiconductor electron affinity, χ. E_c, E_F, and E_V are the conduction band minimum, Fermi level, and valence band maximum, respectively. Black lines show the system under no bias, and the blue and red lines show the system under a forward bias, V_{For}, and a reverse bias, V_{Rev}, respectively. V_D is the depletion potential. The valence bands are omitted because we are working with an n-type semiconductor. (i) When a forward bias is applied, a current I_{For} is produced by thermally excited electrons crossing into the metal over the barrier. (ii) When a reverse bias is applied, a current I_{Rev} is produced by thermally assisted tunneling of electrons from the metal. (b) Key point in conduction occurring at a saddle point in the conduction band minimum, $E_c(F,\mathbf{r})$. As shown schematically, electrons may take different paths through the space-varying E_c, starting at different points and (i) crossing over or (ii) tunneling through the same barrier—a variational calculus problem. In both cases, the current follows paths that (i) cross-over or (ii) tunnel through the inflection point.

bias, electrons in the semiconductor enter the metal by thermionic emission over a barrier of height ϕ. The Schottky−Mott barrier height, unmodified by strain, defects, interfacial charge redistribution, or external potentials, is $\phi_0 = \Phi_m − \chi$, where Φ_m is the work function of the metal and χ is the electron affinity of the semiconductor.[53,54]

For forward bias using standard thermionic emission theory[50] and electromechanical band bending, with the assumption that $V \gg k_B T/q$, the current as a function of both bias and applied force, F, is

$$I_F(V, F) = A(F)B^*T^2 \exp\left(-\frac{q\phi}{k_B T}\right)$$
$$\times \exp\left(-\frac{q(V/n + V^{EM}(F))}{k_B T}\right) \tag{1}$$

where $A(F)$ is the contact area, B^* the Richardson constant, T the temperature, q the electron charge, k_B the Boltzmann constant, $V^{EM}(F)$ the potential due to electromechanical terms, and n the ideality factor. It is convenient to substitute $\phi^{eff}(F) = \phi + V^{EM}(F)$.

The area $A(F)$ was modeled by a sphere-half-space Hertzian contact[51] as

$$A(F) = \pi \left(\frac{3RF}{2E^*} \right)^{2/3} \tag{2}$$

where R is the radius of the sphere (AFM probe tip) and $\frac{1}{E^*} = \frac{1}{2} \left(\frac{1 - \nu_{STO}^2}{E_{STO}} + \frac{1 - \nu_{PtIr}^2}{E_{PtIr}} \right)$, with Young's moduli and Poisson's ratios:[55,56] $E_{STO} = 270$ GPa, $\nu_{STO} = 0.24$, $E_{PtIr} = 230$ GPa, and $\nu_{PtIr} = 0.37$. Values of $A(F)$ range from 300 to 900 nm^2 for the experiments herein.

With $A(F)$ determined, $\phi^{eff}(F)$ and the ideality factor n were directly fit to each forward-bias $I-V$ curve using eq 1. We assumed $B^* = 156$ A cm^{-2} K^{-2} for Nb:STO samples,[57] and room temperature, $T = 295$ K. Details of the fitting are in the Supporting Information (Section SN4). By plotting ϕ^{eff} as a function of the force, Figure 3a condenses the forward bias
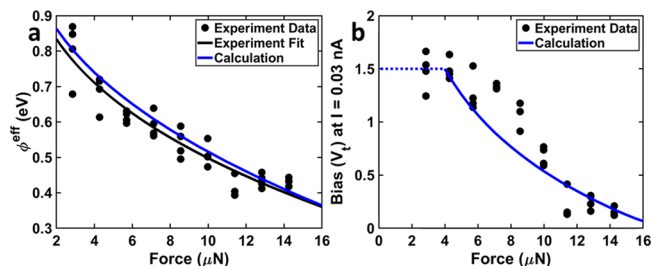

Figure 3. Comparison of the experimental and calculated effective barriers (forward) and threshold biases (reverse). (a) Experimental effective barrier heights, ϕ^{eff}, plotted against the tip force, F (dots), with a curve fit (black line) of the form $\phi_0 - bF^{1/3}$, with $\phi_0 = 1.31 \pm 0.10$ eV and $b = -0.38 \pm 0.05$ eV/μN$^{1/3}$ and the numerically calculated barrier (blue line). (b) Experimental (black dots) and calculated (solid blue line) threshold biases, $V_{Rev,t}$, at a threshold current of $I = 0.03$ nA in reverse bias. The experimental data suggest a breakdown bias of 1.5 V (dotted blue line).

data presented in Figure 1. (Figure 3b does the same for the reverse bias data and is discussed later.) Fitting ϕ^{eff} gave $\phi^{eff}(F) = \phi_0 + bF^{1/3}$ with $\phi_0 = 1.31 \pm 0.10$ eV and $b = -0.38 \pm 0.05$ eV/μN$^{1/3}$ (95% confidence intervals), plotted in Figure 3a. This Hertzian-type $F^{1/3}$ scaling matches previous calculations[31] and experimental observations of tribocurrents.[58] The average value of the ideality factor n was 2.04 ± 0.09 (95% confidence interval). Ideality factors of 1−2 are appropriate depending upon carrier details;[50] values of $n = 1.2-1.8$ have been observed[59] for progressively decreasing interface quality, and an AFM tip contact is expected to be a low-quality interface. The intercept, ϕ_0, is the unmodified barrier height and, in the Schottky−Mott limit, is the difference between the PtIr work function, Φ_m, and the unmodified STO electron affinity, χ_0. For STO, the electron affinity is approximately[60] $\chi_0 = 4$ eV. Though we find no reports of Φ_m, it is bound by[61−63] $\Phi_{Pt} = 5.6$ eV and $\Phi_{Ir} = 4.65$ eV. Using a simple linear interpolation, $\Phi_m = 0.8\Phi_{Pt} + 0.2\Phi_{Ir} = 5.4$ eV. From this, we expect the intercept to be 1.4 eV, close to the experimental result.

We now turn to modeling the effective barrier $\phi^{eff}(F)$, with force F. Assuming cylindrical symmetry, we consider the conduction band energy, $E_c(F,\mathbf{r})$, as a function of applied force and position, $\mathbf{r} = (\rho,z)$. Assuming that metal work function shifts due to strain are relatively small,[64] then

$$E_c(F, \mathbf{r}) - E_F = V^{EM}(F, \mathbf{r}) + q\Phi_{DEP}(\mathbf{r}) + q\Phi_{IMG}(F, \mathbf{r}) \tag{3a}$$

$$V^{EM}(F, \mathbf{r}) = \frac{dE_c}{d\varepsilon}\varepsilon(F, \mathbf{r}) + q\Phi_{FXE}(F, \mathbf{r}) \tag{3b}$$

Equation 3b has two electromechanical terms on the right: the first is the deformation potential and average Coulomb potential shift due to strain (which includes "surface" effects as described later[48]); the second is the flexoelectric potential. The other terms on the right in eq 3a are conventional diode contributions: the second term is the depletion potential in the doped STO and the third the image potential for an electron crossing the semiconductor−metal interface. Since STO is centrosymmetric, we do not include any piezoelectric terms.

We use analytical solutions of Hertzian contact theory for a PtIr sphere with radius R indenting an STO half-space to calculate the strains and strain gradients. First, we consider the effects of strain without any gradients, which can be split into two terms, a volumetric strain and the remaining deviatoric shear strain. While volumetric strains modify the conduction band level uniformly, the shear strains cause band splitting,[65] lifting degeneracies. We will consider only the volumetric strains, ε_{vol}, and assume that the band splitting cancels on average. The quantity of interest is then

$$\frac{dE_c}{d\varepsilon} \approx \frac{d}{d\varepsilon_{vol}}(E_c - \overline{V}) + \frac{d}{d\varepsilon_{vol}}(\overline{V} - E_{vac}) = D_{BS}^C + \varphi \tag{4}$$

where $\overline{V}$ is the average Coulomb potential in the crystal, and we split $\frac{dE_c}{d\varepsilon}$ into two known derivatives. The first, the strain-induced change in the conduction band level, is the conduction-band-specific deformation potential, D_{BS}^C, as described by Stengel.[66] This term describes the shift of the conduction band edge with respect to $\overline{V}$, so we must also consider how the mean inner potential, $\overline{V} - E_{vac}$, changes with strain. The important mean inner potential term has often been called a "surface flexoelectric" contribution,[48,66] but we prefer an interpretation consistent with electron diffraction, as discussed recently.[48] This is the second term in eq 4, φ, and is determined using the Ibers approximation,[48,67−69] which is accurate to ∼10%. Thus, we have

$$\frac{dE_c}{d\varepsilon} \approx D_{BS}^C + \varphi = -17.2 \text{ eV} + 22.2 \text{ eV} = 5 \text{ eV} \tag{5}$$

Returning to eq 3, we next consider the bulk flexoelectric response. The polarization, P, due to the strain gradient is

$$P_i(F, \mathbf{r}) = \epsilon_{STO} f_{ijkl} \frac{d\varepsilon_{kl}(F, \mathbf{r})}{dx_j} \tag{6}$$

where f_{ijkl} is the flexocoupling tensor and ϵ_{STO} is the permittivity. We assume cubic symmetry , with the values[70,71] for STO: $f_{1111} = -11.4$ V, $f_{1122} = -12.4$ V, and $f_{1212} = -0.4$ V. The potential is therefore

$$\Phi_{FXE}(F, \mathbf{r}) = \frac{1}{4\pi} \int_\Omega f_{ijkl} \frac{d\varepsilon_{kl}(F, \mathbf{r}')}{dx_j} \cdot \frac{\mathbf{r} - \mathbf{r}'}{|\mathbf{r} - \mathbf{r}'|^3} d\mathbf{r}' \tag{7}$$

Beyond electromechanical effects, the applied bias and the formation of a depletion region near the surface of doped STO must both be accounted for in Φ_{DEP}. We assume Φ_{DEP} follows the form given for Nb-doped STO by Yamamoto et al.,[71] depending only upon the distance z from the surface:
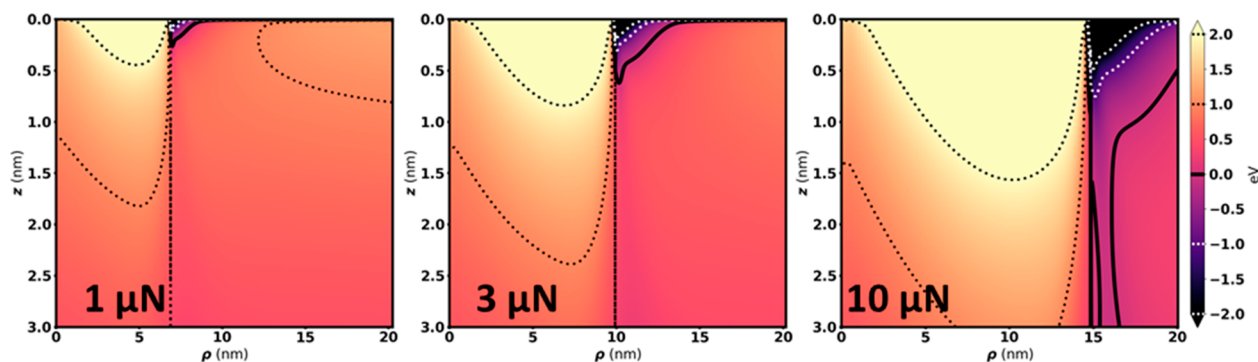
Figure 4. Calculated conduction band minima for different forces. Calculated $E_c(F, \mathbf{r}) - E_F$ for tip radius $R = 60$ nm and three different forces using cylindrical polars with z into the STO and ρ radial. The unstrained bulk conduction band minimum is marked by 0 eV. Contour lines are marked on the color bar.

$$\Phi_{\text{DEP}}(\mathbf{r}) = \frac{\sqrt{a}\, b\epsilon_0}{qN} \left\{ \cosh\left[\cosh^{-1}\left(1 + \frac{qN}{\sqrt{a}\, b\epsilon_0} V_d \right) - \frac{qN}{b\epsilon_0} z \right] - 1 \right\}$$
$$+ \left(V/n - (E_F - E_c) \right) \tag{8}$$

where N is the dopant concentration and a and b parametrize the field (ε) dependence of the effective permittivity of STO as $\epsilon_{\text{STO}} = b\epsilon_0/\sqrt{a + \varepsilon^2}$ and have values 1.64×10^{15} V^2/m^2 and 1.48×10^{10} V/m, respectively, at room temperature,[71] $V_d = \phi_0 + E_F - E_c - V/n$ is the diffusion potential, and V is the applied potential. The effective field-dependent permittivity accounts for self-consistent interactions between the field-dependence and strain-dependence of the permittivity, electrostriction, changes in the screening due to carriers in the conduction band, and other possible terms relevant near a nominally unstrained Schottky diode interface, and has been shown to match experimental results of Pt/STO Schottky diodes.[71−74] Further discussion of issues in the evaluation of the band bending, including how the permittivity varies, is available in the Supporting Information (Section SN14). We included the image charge potential, Φ_{IMG}, generated as the electrons approach the surface of the semiconductor; however, it is very small relative to the other terms (see the Supporting Information (Section SN6)).

Therefore, for E_c,

$$E_c(F, \mathbf{r}) - E_F = (D_{\text{BS}}^C + \varphi)\varepsilon(F, \mathbf{r})$$
$$+ \frac{1}{4\pi} \int_\Omega f_{ijkl} \frac{d\varepsilon_{kl}(F, \mathbf{r}')}{dx_j} \cdot \frac{\mathbf{r} - \mathbf{r}'}{|\mathbf{r} - \mathbf{r}'|^3} \, d\mathbf{r}'$$
$$+ \Phi_{\text{DEP}}(\mathbf{r}) \tag{9}$$

The total band bending (radially symmetric) is shown in Figure 4 for three representative forces. To compare with the experimental results, ϕ^{eff} was then calculated numerically by considering the paths an electron may take through the STO to the interface—a variational calculus problem. For a given path, the barrier is the maximum value of E_c along that path. There is a non-uniform barrier, a function of ρ, which is the minimum of the barriers of the possible paths to that point at the interface. Finally, a single-valued ϕ^{eff} was calculated from

this non-uniform barrier. These calculations indicate that the current flows through a thin ring just inside the edge of contact, where there is a saddle point in the potential. Note that under the center of the tip ($\rho = 0$) the strains are large, but, by symmetry, the gradients are zero, whereas the largest strain gradients are near the contact edge. Further details of the calculation appear in the Supporting Information (Section SN7). One consequence of a non-uniform barrier is its direct effect on the non-ideality of the diode.[75] According to our calculations, this accounts for some, but not all, of the non-ideality (see the Supporting Information (Section SN13)). The remaining non-ideality is likely caused by other sources, such as in-gap states. The results for the effective barrier are shown in Figure 3a and are in excellent agreement with the experimental data.

Turning next to the reverse bias case, we considered a reverse threshold bias, $V_{\text{Rev,t}}$, at which the current reaches some threshold magnitude, $|I(V_t)| = I_t$ (see Figure 3b). The value $I_t = 0.03$ nA was just large enough to avoid instrumental noise (as seen in the Supporting Information Section SN8) this localizes the current to a small region and reduces the range of different tunneling barrier heights that contribute. We calculate the current by integrating for fixed radial values across the thermally assisted tunneling barrier defined by the maximum of the STO conduction band and the metal Fermi level. This neglects the charge transfer that can occur with electrons moving from the metal into the STO very close to the tip. The current density is[76]

$$J_{\text{Tun}}(V, F, \rho) = \frac{B^* T}{k_B} \int_0^{\phi_{\text{max}}^{\text{eff}}} P_{\text{Tun}}(E_m, V, F, \rho)$$
$$\times \ln\left[\frac{1 + \exp(-(E_m + \xi_F)/k_B T)}{1 + \exp(-(E_m + \xi_F + qV)/k_B T)} \right] dE_m \tag{10}$$

where $P_{\text{Tun}}(E_m, V, F, \rho)$ is the tunneling probability for an electron with energy E_m, where $E_m = 0$ is the metal Fermi level and $\xi_F = (E_F - E_C)$. This is a general form that includes thermally assisted tunneling. Using the first-order WKB approximation,[77] where a derivative term absent in the zero-order WKB is included,
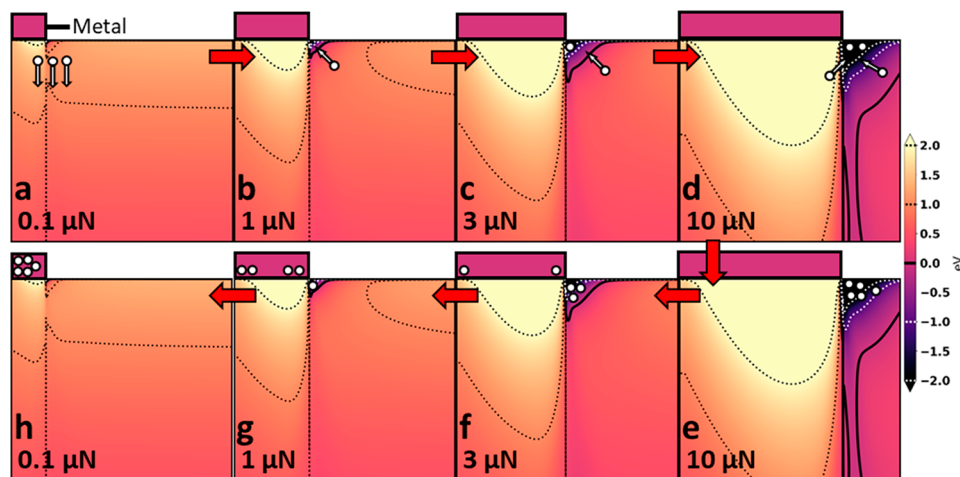
Figure 5. Ratcheting mechanism for charge transfer in metal−semiconductor contacts. (a−h) $E_c(F,\mathbf{r}) - E_F$ in the ranges $0 \le \rho \le 20$ nm and $0 \le z \le 3$ nm for increasing and decreasing forces, F, as in contact and pull-off of an asperity. (a) For very low forces, the depletion potential is most important. (b−d) As the force increases, electrons (white circles, schematically arrowed) move from regions with an increasing potential to regions with decreasing potential. (e−g) As the force decreases, the number of available states in the potential well decreases, forcing some electrons into the metal rather than back across the barrier in the semiconductor, where states near the metal Fermi level $E_{F,M} = 0$ are available. (h) After the force is completely released, electrons have transferred to the metal.

$$P_{\text{Tun}}(E_m, V, F, \rho) = \exp\left[-2\int_C \left(\frac{2m^*}{\hbar^2}(\phi^{\text{eff}}(V, F, \mathbf{r}) - E_m) + \frac{1}{\sqrt{\frac{8m^*}{\hbar^2}(\phi^{\text{eff}}(V, F, \mathbf{r}) - E_m)}}\frac{d}{d\mathbf{r}}\phi^{\text{eff}}(V, F, \mathbf{r})\right)^{1/2} d\mathbf{r}\right]$$

$$(11)$$

where m^* is the STO conduction band effective mass, C is a path from the interface at radius ρ to a point in the STO far away (where E_c is constant), and the derivative is defined such that it is positive when ϕ^{eff} is increasing. Including the gradient term captures the quickly varying potential near the contact; its effect is mostly less than 15%, increasing at larger forces. Of the possible paths, that with the highest tunneling probability determines P_{Tun}—another variational calculus problem.

The experimentally observed current at the threshold applied bias, $V_{\text{Rev,t}}$, and tip force, F, is given by eq 12.

$$I(V_{\text{Rev,t}}, F) = I_t = \int_0^{\rho_{\max}} J_{\text{Tun}}(V_{\text{Rev,t}}, F, \rho) 2\pi\rho \, d\rho \qquad (12)$$

By restricting the analysis to low currents, the thermally assisted tunneling is almost exclusively through the lowest part of the barrier near the edge of the contact region, the same location of current flow calculated in the forward bias case. At higher currents, the tunneling occurs over a larger region (see the Supporting Information (Section SN8)).

A plot of $V_{\text{Rev,t}}$ with respect to F is shown in Figure 3b. The calculations and the experimental data agree well except for reverse biases above 1.5 V. This can be attributed to a force-independent breakdown: in addition to the system missing the guard rings of modern Schottky devices,[78] the sharp radius of curvature of the interface and the relatively high doping level of the STO both suggest breakdown is possible.[79]

The experimental results and modeling herein are in excellent agreement, well within the experimental limits. The analysis contains two unknown parameters, the ideality of the diode in forward and reverse bias and the value for the Schottky barrier; all other terms in the model are either known or are calculated ab initio. For any specific system, the details

will depend on many terms, including the flexoelectric terms, temperature, elastic constants, and differences in work function. The Supporting Information (Sections SN10 and SN12) discusses the contributions of the strain gradient and polarization components, and the contributions of the terms in eqs 4, 7, and 8.

One point of some importance is that we obtained good agreement between experiment and calculations without having atomically ordered and clean surfaces. This is because the barriers are beneath the surface by 1−3 nm (see the Supporting Information (Section SN7)). This means that the behavior of a particular material will be somewhat consistent, which is what has been found experimentally. Of course, chemisorbed polar molecules or water will have an effect on the zero-force barrier, but they will have less effect on the band-bending changes.

Though the calculations do not explicitly address charge transfer, they offer some insights that agree with experiments for sliding Schottky generator experiments[43,52] that observe electron transfer from a semiconductor to a metal, surprisingly independent of the sign of the flexocoupling coefficients and details of shear versus indentation or plowing. What one has is a type of ratcheting charge pump. More details are in the Supporting Information (Section SN11); we will summarize here and in Figure 5. Near the contact there is a region where the bands bend down in the semiconductor as force is applied; these regions will pull in electrons from the body of the semiconductor far from the contact region. As the force is released, there is a barrier for these electrons to move back into the semiconductor, so transfer to the metal is favored. Changing the sign of the flexocoupling coefficients will change whether this downward region is outside or inside the contact,

not its presence. Similarly, details of shear versus compression or other types of contact will change the exact magnitude of the region where the band bends significantly down, but the overall details will remain the same.

We have presented a model of electromechanical band bending in a triboelectric metal−semiconductor system that quantitatively agrees with force-dependent current−bias experiments and qualitatively agrees with charge transfer observed in other works. This offers insight into the details of the triboelectric effect in metal−semiconductor systems and provides strong evidence of the importance of flexoelectric band bending in triboelectricity. Complex mechanics, band-bending physics, and device physics combine to end up producing a relatively simple and quite general result. While details will be dependent upon specifics of the materials, broad-brush results for charge transfer are surprisingly invariant of, for instance, the amount of shear at the contact. If this was not the case, then the simple concepts such as the 19th century triboelectric series would never have had even limited success.

Is triboelectricity as a ratcheting charge pump generalizable from the Schottky contacts herein to other cases? Perhaps.

ASSOCIATED CONTENT

ⓈⒾ Supporting Information

The Supporting Information is available free of charge at https://pubs.acs.org/doi/10.1021/acs.nanolett.2c00107.

> Further details on the experimental methods, data analysis, and numerical calculations; additionally, descriptions of measures taken to ensure the quality of the experimental data, more calculation results, and detailed support for the triboelectric ratcheting argument (PDF)

AUTHOR INFORMATION

Corresponding Author

Laurence D. Marks − *Department of Materials Science and Engineering, Northwestern University, Evanston, Illinois 60201, United States of America;* ⓞ orcid.org/0000-0002-6659-2016; Email: l-marks@northwestern.edu

Authors

Karl P. Olson − *Department of Materials Science and Engineering, Northwestern University, Evanston, Illinois 60201, United States of America;* ⓞ orcid.org/0000-0001-5339-1883

Christopher A. Mizzi − *Department of Materials Science and Engineering, Northwestern University, Evanston, Illinois 60201, United States of America;* ⓞ orcid.org/0000-0002-4209-854X

Complete contact information is available at:
https://pubs.acs.org/10.1021/acs.nanolett.2c00107

Author Contributions

K.P.O. performed the experiments and analysis with advice from C.A.M. and supervision from L.D.M. All authors contributed to the writing of the Letter.

Notes

The authors declare no competing financial interest.

ACKNOWLEDGMENTS

■ REFERENCES

(1) Watanabe, H.; et al. Triboelectrification of pharmaceutical powders by particle impact. *Int. J. Pharm.* **2007**, *334*, 149−155.

(2) Wong, J.; Kwok, P. C. L.; Chan, H.-K. Electrostatics in pharmaceutical solids. *Chem. Eng. Sci.* **2015**, *125*, 225−237.

(3) Naik, S.; et al. Quantification of Tribocharging of Pharmaceutical Powders in V-Blenders: Experiments, Multiscale Modeling, and Simulations. *J. Pharm. Sci.* **2016**, *105*, 1467−1477.

(4) Fan, F.-R.; et al. Transparent Triboelectric Nanogenerators and Self-Powered Pressure Sensors Based on Micropatterned Plastic Films. *Nano Lett.* **2012**, *12*, 3109−3114.

(5) Niu, S. M.; et al. Theoretical study of contact-mode triboelectric nanogenerators as an effective power source. *Energy Environ. Sci.* **2013**, *6*, 3576−3583.

(6) Dharmasena, R. D. I. G.; et al. Triboelectric nanogenerators: providing a fundamental framework. *Energy Environ. Sci.* **2017**, *10*, 1801−1811.

(7) Wang, J.; et al. Achieving ultrahigh triboelectric charge density for efficient energy harvesting. *Nat. Commun.* **2017**, *8*, 88.

(8) Liu, J.; et al. Direct-current triboelectricity generation by a sliding Schottky nanocontact on MoS2 multilayers. *Nat. Nanotechnol.* **2018**, *13*, 112−116.

(9) Yang, R.; et al. Semiconductor-based dynamic heterojunctions as an emerging strategy for high direct-current mechanical energy harvesting. *Nano Energy* **2021**, *83*, 105849.

(10) Schmidt, D. S.; Schmidt, R. A.; Dent, J. D. Electrostatic force in blowing snow. *Bound.-Layer Meteorol.* **1999**, *93*, 29−45.

(11) Mather, T. A.; Harrison, R. G. Electrification of volcanic plumes. *Surv. Geophys.* **2006**, *27*, 387−432.

(12) Forward, K. M.; Lacks, D. J.; Sankaran, R. M. Particle-size dependent bipolar charging of Martian regolith simulant. *Geophy. Res. Lett.* **2009**, *36*, L13201.

(13) Pähtz, T.; Herrmann, H. J.; Shinbrot, T. Why do particle clouds generate electric charges? *Nat. Phys.* **2010**, *6*, 364−368.

(14) Zheng, X. J. Electrification of wind-blown sand: recent advances and key issues. *Eur. Phys. J. E* **2013**, *36*, 138.

(15) Davis, M. S.; Madani, M. R. Investigation into the Effects of Static Electricity on Wind Turbine Systems. *Proc. 2018 6th Int. Renew. Sustain. Energy Conf. IRSEC* **2018**, 1−7.

(16) Jachowicz, J.; Wissurel, G.; Garcia, M. L. Relationship between Triboelectric Charging and Surface Modifications of Human Hair. *J. Soc. Cosmet. Chem.* **1985**, *36* (3), 189−212.

(17) Lodge, R. A.; Bhushan, B. Surface potential measurement of human hair using Kelvin probe microscopy. *J. Vac. Sci. Technol. A* **2007**, *25*, 893−902.

(18) Steinpilz, T.; et al. Electrical charging overcomes the bouncing barrier in planet formation. *Nat. Phys.* **2020**, *16*, 225−229.

(19) Shaw, P. E. Experiments on tribo-electricity. I.-The tribo-electric series. *Proc. R. Soc. London A* **1917**, *94*, 16−33.

(20) Richards, H. F. The contact electricity of solid dielectrics. *Phys. Rev.* **1923**, *22*, 122−133.

(21) Harper, W. R. The Volta effect as a cause of static electrification. *Proc. R. Soc. London A* **1951**, *205*, 83−103.

(22) Montgomery, D. J. Static Electrification of Solids. *Solid State Phys.* **1959**, *9*, 139−197.

(23) Harper, W. R. Contact Electrification of Semiconductors. *Br. J. Appl. Phys.* **1960**, *11*, 324−331.

(24) Harper, W. R. *Contact and Frictional Electrification*; Oxford University Press, 1967.

(25) Liu, C. Y.; Bard, A. J. Electrostatic electrochemistry at insulators. *Nat. Mater.* **2008**, *7*, 505−509.

(26) Lowell, J.; Rose-Innes, A. C. Contact electrification. *Adv. Phys.* **1980**, *29*, 947−1023.

(27) Davies, D. K. Charge Generation on Dielectric Surfaces. *J. Phys. D: Appl. Phys.* **1969**, *2*, 1533−1537.

(28) Diaz, A. F.; Fenzel-Alexander, D. An Ion Transfer Model for Contact Charging. *Langmuir* **1993**, *9*, 1009−1015.

(29) McCarty, L. S.; Whitesides, G. M. Electrostatic charging due to separation of ions at interfaces: contact electrification of ionic electrets. *Angew. Chem., Int. Ed. Engl.* **2008**, *47*, 2188−2207.

(30) Baytekin, H. T.; Baytekin, B.; Incorvati, J. T.; Grzybowski, B. A. Material transfer and polarity reversal in contact charging. *Angew. Chem., Int. Ed. Engl.* **2012**, *51*, 4843−4847.

(31) Mizzi, C. A.; Lin, A. Y. W.; Marks, L. D. Does Flexoelectricity Drive Triboelectricity? *Phys. Rev. Lett.* **2019**, *123*, 116103.

(32) Mizzi, C. A.; Marks, L. D. How Flexoelectricity Drives Triboelectricity. *arXiv (Condensed Matter: Materials Science)*, 2020, 2010.12963v1. https://arxiv.org/abs/2010.12963 (accessed 2022-02-23).

(33) Terris, B. D.; Stern, J. E.; Rugar, D.; Mamin, H. J. Contact electrification using force microscopy. *Phys. Rev. Lett.* **1989**, *63*, 2669−2672.

(34) Jeffery, S.; Sofield, C. J.; Pethica, J. B. The influence of mechanical stress on the dielectric breakdown field strength of thin SiO_2 films. *Appl. Phys. Lett.* **1998**, *73*, 172−174.

(35) Vick, F. A. Theory of contact electrification. *B. J. Appl. Phys.* **1953**, *4*, S1−S5.

(36) Kalinin, S. V.; Karapetian, E.; Kachanov, M. Nanoelectromechanics of piezoresponse force microscopy. *Phys. Rev. B* **2004**, *70*, 184101.

(37) Abdollahi, A.; Domingo, N.; Arias, I.; Catalan, G. Converse flexoelectricity yields large piezoresponse force microscopy signals in non-piezoelectric materials. *Nat. Commun.* **2019**, *10*, 1266.

(38) Sun, L.; Zhu, L.; Zhang, C.; Chen, W.; Wang, Z. Mechanical Manipulation of Silicon-based Schottky Diodes via Flexoelectricity. *Nano Energy* **2021**, *83*, 105855.

(39) Das, S.; et al. Controlled manipulation of oxygen vacancies using nanoscale flexoelectricity. *Nat. Commun.* **2017**, *8*, 615.

(40) Park, S. M.; et al. Selective control of multiple ferroelectric switching pathways using a trailing flexoelectric field. *Nat. Nanotechnol.* **2018**, *13*, 366−370.

(41) Yang, M.-M.; Kim, D. J.; Alexe, M. Flexo-photovoltaic effect. *Science* **2018**, *360*, 904−907.

(42) Wang, L.; et al. Flexoelectronics of centrosymmetric semiconductors. *Nat. Nanotechnol.* **2020**, *15*, 661−667.

(43) Yang, R. Z.; Benner, M.; Guo, Z. P.; Zhou, C.; Liu, J. High-Performance Flexible Schottky DC Generator via Metal/Conducting Polymer Sliding Contacts. *Adv. Funct. Mater.* **2021**, *31*, 2103132.

(44) Meng, J.; et al. Triboelectric Nanogenerator Enhanced Schottky Nanowire Sensor for Highly Sensitive Ethanol Detection. *Nano Lett.* **2020**, *20*, 4968−4974.

(45) Kim, M.; et al. MoS_2 triboelectric nanogenerators based on depletion layers. *Nano Energy* **2019**, *65*, 104079.

(46) Olsen, M.; et al. Schottky model for triboelectric temperature dependence. *Sci. Rep.* **2018**, *8*, 5293.

(47) Park, S. M.; et al. Flexoelectric control of physical properties by atomic force microscopy. *Appl. Phys. Lett.* **2021**, *8*, 041327.

(48) Mizzi, C. A.; Marks, L. D. The role of surfaces in flexoelectricity. *J. Appl. Phys.* **2021**, *129*, 224102.

(49) Colinge, J. P.; Colinge, C. A. *Physics of Semiconductor Devices*; Springer Science + Business Media, 2005; pp 139−152. DOI: 10.1007/0-306-47622-3_5.

(50) Sze, S. M.; Ng, K. K. *Physics of Semiconductor Devices*, 3rd ed.; John Wiley & Sons, 2007; pp 134−196. DOI: 10.1002/0470068329.

(51) Hertz, H. Ueber die Berührung fester elastischer Körper. *J. Reine Angew. Math.* **1882**, *1882*, 156−171.

(52) Huang, X. Y.; et al. Microscale Schottky superlubric generator with high direct-current density and ultralong life. *Nat. Commun.* **2021**, *12*, 2268.

(53) Schottky, W. Zur Halbleitertheorie der Sperrschicht- und Spitzengleichrichter. *Z. Phys.* **1939**, *113*, 367−414.

(54) Mott, N. F. The theory of crystal rectifiers. *Proc. R. Soc. London A* **1997**, *171*, 27−38.

(55) Bertelsen, B. B. I. The U. S. Motor Vehicle Emission Control Programme. *Platinum Metals Rev.* **2001**, *45*, 50−59.

(56) Bell, R. O.; Rupprecht, G. Elastic Constants of Strontium Titanate. *Phys. Rev.* **1963**, *129*, 90−94.

(57) Rana, K. G.; Khikhlovskyi, V.; Banerjee, T. Electrical transport across Au/Nb:SrTiO 3 Schottky interface with different Nb doping. *Appl. Phys. Lett.* **2012**, *100*, 213502.

(58) Escobar, J. V.; Chakravarty, A.; Putterman, S. J. Effect of anodic oxidation of single crystal boron doped diamond on tribocurrent and macroscopic friction force with metals. *Diamond Relat. Mater.* **2013**, *36*, 8−15.

(59) Mikheev, E.; Hoskins, B. D.; Strukov, D. B.; Stemmer, S. Resistive switching and its suppression in Pt/Nb:SrTiO3 junctions. *Nat. Commun.* **2014**, *5*, 3990.

(60) Chien, T.; et al. Built-in electric field induced mechanical property change at the lanthanum nickelate/Nb-doped strontium titanate interfaces. *Sci. Rep.* **2016**, *6*, 19017.

(61) Ishii, R.; Matsumura, K.; Sakai, A.; Sakata, T. Work function of binary alloys. *Appl. Surf. Sci.* **2001**, *169−170*, 658−661.

(62) Lin, S. F.; Pierce, D. T.; Spicer, W. E. Photoemission Studies of Platinum. *Phys. Rev. B* **1971**, *4*, 326−329.

(63) Arthur, J. R.; Hansen, R. S. Study of the Adsorption of Hydrogen, Ethane, Ethylene, and Acetylene on Iridium by Field Emission Microscopy. *J. Chem. Phys.* **1962**, *36*, 2062−2071.

(64) Wang, X. F.; et al. The canonical work function-strain relationship of the platinum metal: A first-principles approach to metal-gate transistor optimization. *Appl. Phys. Lett.* **2013**, *102*, 223504.

(65) Van De Walle, C. G. Band lineups and deformation potentials in the model-solid theory. *Phys. Rev. B* **1989**, *39*, 1871−1883.

(66) Stengel, M. From flexoelectricity to absolute deformation potentials: The case of SrTiO3. *Phys. Rev. B* **2015**, *92*, 205115.

(67) Rez, D.; Rez, P.; Grant, I. Dirac−Fock calculations of X-ray scattering factors and contributions to the mean inner potential for electron scattering. *Acta Crystallogr.* **1994**, *A50*, 481−497.

(68) O'Keeffe, M.; Spence, J. C. H. On the average Coulomb potential (Φ_0) and constraints on the electron density in crystals. *Acta Crystallogr.* **1994**, *A50*, 33−45.

(69) Ibers, J. A. Atomic scattering amplitudes for electrons. *Acta Crystallogr.* **1958**, *11*, 178−183.

(70) Hong, J. W.; Vanderbilt, D. First-principles theory and calculation of flexoelectricity. *Phys. Rev. B* **2013**, *88*, 174107.

(71) Yamamoto, T.; Suzuki, S.; Kawaguchi, K.; Takahashi, K. Temperature dependence of the ideality factor of Ba1-xKxBiO3/Nb-doped SrTiO3 all-oxide-type Schottky junctions. *Jpn. J. Appl. Phys.* **1998**, *37*, 4737−4746.

(72) Yamamoto, T.; et al. Effect of the Field Dependent Permittivity and Interfacial Layer on Ba1-xKxBiO3/Nb-Doped SrTiO3 Schottky Junctions. *Jpn. J. Appl. Phys.* **1997**, *36*, L390−L393.

(73) Ohashi, N.; et al. Determination of Schottky barrier profile at Pt/SrTiO3:Nb junction by x-ray photoemission. *Appl. Phys. Lett.* **2012**, *101*, 251911.

(74) Hirose, S.; et al. Electric field and temperature dependence of dielectric permittivity in strontium titanate investigated by a photoemission study on Pt/SrTiO3:Nb junctions. *Appl. Phys. Lett.* **2015**, *106*, 191602.

(75) Tung, R. T. Electron transport of inhomogeneous Schottky barriers. *Appl. Phys. Lett.* **1991**, *58*, 2821−2823.

(76) Eriksson, J.; Rorsman, N.; Zirath, H. 4H-silicon carbide schottky barrier diodes for microwave applications. *IEEE Trans. Microwave Theory Tech.* **2003**, *51*, 796−804.

(77) Latreche, A. Modified expressions of field and thermionic-field emission for Schottky barrier diodes in the reverse regime. *Semicond. Phys. Quant.* **2021**, *24*, 16−21.

(78) Lepselter, M. P.; Sze, S. M. Silicon Schottky Barrier Diode with Near-Ideal I-V Characteristics. *Bell Syst. Technol. J.* **1968**, *47*, 195−208.

(79) Sze, S. M.; Gibbons, G. Effect of junction curvature on breakdown voltage in semiconductors. *Solid-State Electron.* **1966**, *9*, 831−845.